Title

High contrast dual-mode optical and 13C magnetic resonance imaging in diamond particles

Authors

Lv, X
Walton, JH
Druga, E
et al.

Publication Date

2019-09-04

Peer reviewed

High contrast dual-mode optical and ^{13}C magnetic resonance imaging in diamond particles

X. Lv,[1] J. H. Walton,[2] E. Druga,[1] F. Wang,[1] A. Aguilar,[1] T. McKnelly,[1] R. Nazaryan,[1] L. Wu,[1]
O. Shenderova,[3] D. B. Vigneron,[4] C. A. Meriles,[5] J. A. Reimer,[6] A. Pines,[1] and A. Ajoy[1,7,*]

[1]*Department of Chemistry, University of California, Berkeley, California 94720, USA.*
[2]*Nuclear Magnetic Resonance Facility, University of California Davis, Davis, California 95616, USA.*
[3]*Admas Nanotechnologies, Inc., 8100 Brownleigh Dr, Suite 120, Raleigh, NC, 27617 USA.*
[4]*Department of Radiology and Biomedical Imaging, University of CaliforniaSan Francisco, San Francisco, California 94158, USA.*
[5]*Department of Physics and CUNY-Graduate Center, CUNY-City College of New York, New York, NY 10031, USA.*
[6]*Department of Chemical and Biomolecular Engineering, and Materials Science Division Lawrence Berkeley National Laboratory University of California, Berkeley, California 94720, USA.*
[7]*Department of Chemistry, Carnegie Mellon University, 4400 Fifth Avenue, Pittsburgh, Pennsylvania 15213, USA.*

Multichannel imaging – the ability to acquire images of an object through more than one imaging mode simultaneously – has opened exciting new avenues in several areas from astronomy to biomedicine. Visible optics and magnetic resonance imaging (MRI) offer complimentary advantages of resolution, speed and depth of penetration, and as such would be attractive in combination. In this paper, we take first steps towards marrying together optical and MR imaging in a class of biocompatible and deployable particulate materials constructed out of diamond. The particles are endowed with a high density of quantum defects (Nitrogen Vacancy centers) that under optical excitation fluoresce brightly in the visible, but also concurrently electron spin polarize, allowing the hyperpolarization of lattice ^{13}C nuclei to make the particles over three-orders of magnitude brighter than in conventional MRI. We highlight additional benefits in background-free imaging, demonstrating lock-in suppression by factors of 2 and 5 in optical and MR domains respectively, although ultimate limits are at least two orders of magnitude in each domain. Finally, leveraging the ability of optical and MR imaging to simultaneously probe Fourier-reciprocal domains (real and k-space), we elucidate the ability to employ hybrid sub-sampling in both conjugate spaces to vastly accelerate dual-image acquisition, by as much as two orders of magnitude in practically relevant sparse-imaging scenarios. Our work portends new avenues for quantum-enhanced dual-mode imaging platforms and opens possibilities for new therapeutic avenues including in low-field MRI-guided endoscopy.

Introduction – In the quest towards high signal-to-noise (SN) imaging, the power that can be brought to bear by *multimodal* or *multi-messenger* techniques has been long recognized [1, 2]. At its heart such multichannel" imaging entails capturing the object through more than one imaging mode simultaneously, often at widely disparate wavelengths. Exploiting correlations between the different channels portend Kalman filtering approaches [3] that can deliver a high degree of noise or background suppression. Moreover, under appropriate conditions, these correlations engender novel image sampling and reconstruction strategies that can substantially accelerate image acquisition.

While routinely employed in astronomy, a number of these multimodal imaging techniques are now finding compelling applications in biomedicine. For instance, new instruments that combine magnetic resonance imaging (MRI) with radiotherapy have opened exciting new high-precision therapeutic avenues [4]. Interest has gained ground for methods that similarly marry together MRI and optical imaging, with applications in precision 3D MRI-guided laser ablation [5, 6], and in continuously MRI-monitored endoscopy for high-accessibility colorectal cancer screening.

Indeed, in several respects, MRI and optical imaging offer diametrically complementary advantages, a feature that can make them particularly powerful in combination. Visible-wavelength optics is fast, cheap and images at high-resolution; yet often suffers from scattering, attenuation, and aberration distortion when imaging through tissue. MRI, on the other hand, is noninvasive, fully three-dimensional and can be chemically functional; yet it is slow, suffers from weak signals, and offers poor spatial (mm-level) resolution. Perhaps more importantly, optical and MR imaging are carried out in Fourier-reciprocal spaces (x- and k-space). This redundancy immediately makes a combined modality highly persuasive not only are there complementary advantages in sensitivity, resolution and aberration suppression to be gained, but also the possibility for hybrid new image acquisition strategies that sample both real and k-space *simultaneously* to yield meaningful imaging acceleration. If such dual-mode imaging is deployable in a biocompatible and functionally *targetable* material platform, several exciting avenues could result in disease monitoring as well as in targeted drug delivery.

Here we demonstrate proof-of-concept of these gains by showing high contrast dual-mode optical and ^{13}C MRI imaging in diamond microparticles. These versatile materials have gained prominence for tumor targeting given their biocompatiblity and surface functionalizability with antibodies and dendrimers [7–9]. In our work, the diamond particles are incorporated with a large concentration ($\gtrsim$1ppm) of Nitrogen Vacancy (NV) defect centers [10]. Under sub-bandgap illumination $<$575 nm, the particles fluoresce brightly in the red with high luminosity ($\sim$90cd/m^2), with high optical stability, without blinking or bleaching. The NV centers are also endowed with attractive spin properties the generation of fluorescence occurs *concurrently* with the optical polarization of the electron spins associated with them. This macroscopically large polarization ($>$10%) can be transferred to ^{13}C nuclei in the surrounding lattice, *hyperpolarizing* them in vastly athermal states that bequeath them with brightness in MR imaging [11]. We exploit a recent NV-mediated low-field (1-70mT) *room-temperature* hyperpolarization technique [12] that allows large ^{13}C polarization levels ($\sim$1%) and correspondingly high MR signal enhancement factors, over a factor of thousand at 1.5T. Indeed, these gains in MR solid imaging were traditionally possible only through the use of cryogenic conditions and high magnetic fields, and only at substantially lower throughput [13]. Moreover, the ^{13}C polarization can be retained for long periods, approaching $\sim$10min for certain samples at moderate fields $>$100mT [14, 15].

Not only can the high SNR optical and MRI imaging proceed

* ashokaj@berkeley.edu

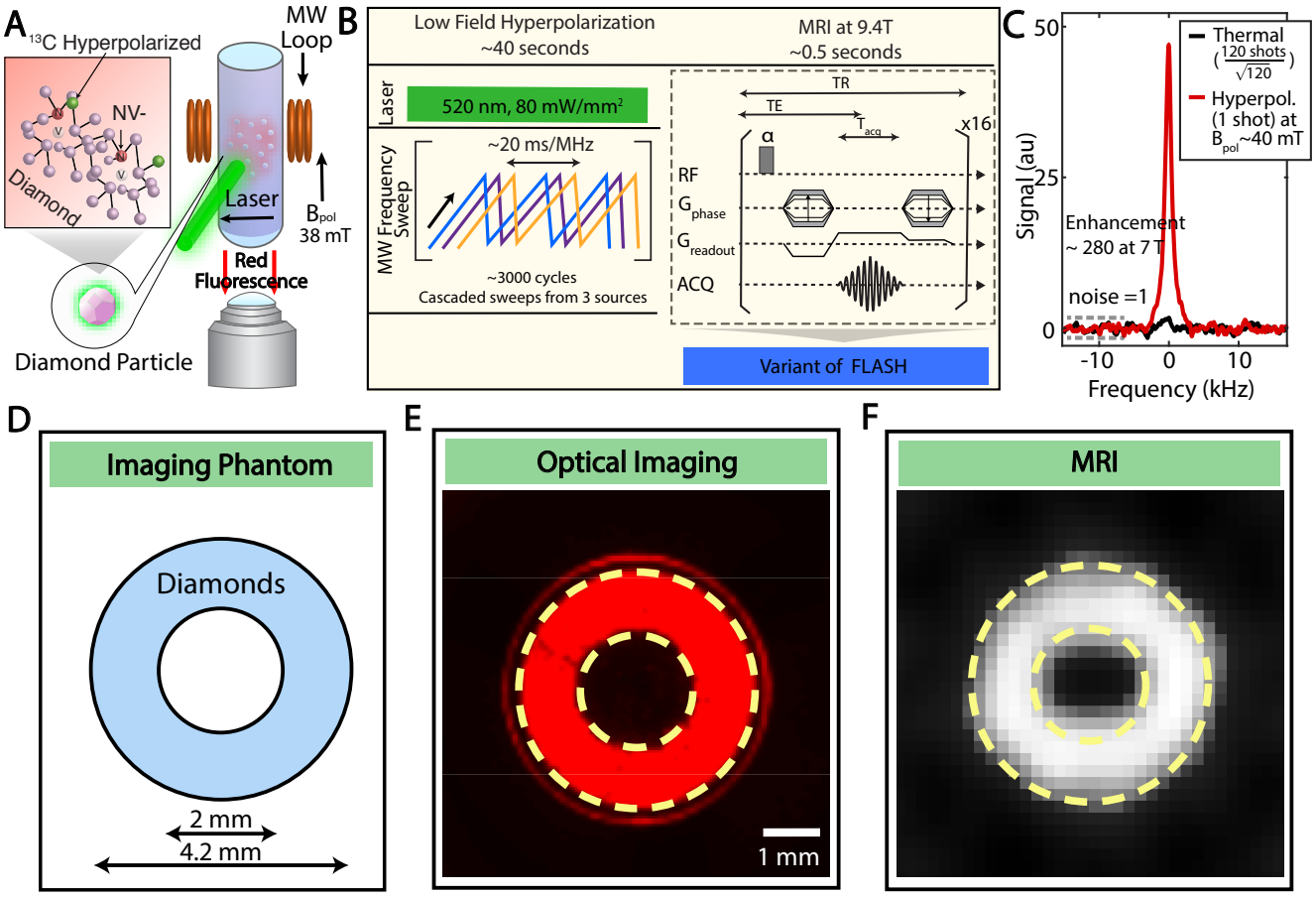

Figure 1. **Dual-mode optical and ^{13}C MR imaging.** (A) *Experiment schematic.* Diamond particles with high-density NV centers are imaged under green (520nm) excitation in fluorescence by a CMOS detector, as well as under ^{13}C MRI through polarization transferred to lattice ^{13}C nuclei from optically polarized NV electrons. (B) *Hyperpolarization and detection protocol.* ^{13}C DNP occurs at low-field ∼38mT under MW sweeps across the NV ESR spectrum. FLASH MR imaging is performed after sample shuttling to 9.4T. Here echo time TE = 0.5ms, repetition time TR = 6ms, acquisition time T_{acq} = 0.36ms. (C) *Typical hyperpolarization signal enhancement*, showing signal gain ≈280±5 against thermal signal at 7T, corresponding to ∼5 orders of magnitude acceleration in MR imaging time. For a fair comparison, the noise in both data is normalized to 1 (dashed lines). (D) Ring shaped phantom filled with 40mg 200μm diamond particles employed for dual-mode imaging. (E) *Fluorescence image* captured through a 594nm long-pass filter. Dashed lines indicate the phantom geometry for reference. (F) *^{13}C MR FLASH image* with 16 averages (≈8s total imaging time), and a square pixel length of 160μm and square FOV with 6.4mm edge.

concurrently, in addition, there is the added advantage that signals from both modes can be *modulated* on-demand, allowing a high degree of background suppression through lock-in techniques [12, 16]. In this manuscript, we demonstrate such high contrast optical and MRI imaging in phantom samples, and show suppression of signal backgrounds by over factors of 2 and 5 respectively in the two imaging dimensions respectively. Crucially, we demonstrate how combined conjugate imaging in real and k-space can promote several orders of magnitudes in imaging acceleration, particularly in wide field-of-view scenarios. Our work paves the way for high contrast, background-free, accelerated dual-mode imaging of biocompatible nanoparticle delivery and targeting agents based on quantum materials.

Dual-mode background-free imaging – Fig. 1A is a schematic of the experiment. Diamond particles (200μm, ∼40mg) arranged in a ring-shaped phantom (Fig. 1D) are imaged optically under continuous 520nm illumination and 630nm long-pass filtering (Fig. 1E). The high intrinsic SNR from the optical florescence is evident, and the ultimate imaging resolution is just diffraction limited. For MR imaging (Fig. 1B,F), we employ dynamic nuclear polarization (DNP) at 38mT to enhance the ^{13}C polarization, and a microcoil in a 9.4T magnet for imaging. The same optical excitation polarizes (initializes to m_s=0) the NV electron spins, and microwave (MW) sweeps across the NV ESR spectrum drive Landau-Zener dynamics that transfers polarization to the ^{13}C nuclei in a fully orientation-independent manner [12, 17, 18]. We obtain ∼0.3% spin polarization in 40s under 1W total optical illumination, and this is primarily laser power limited. At this level, this corresponds to a signal enhancement of 206 times over thermal ^{13}C polarization at 9.4T (Fig. 1C) (∼5× 10^4 over 38mT), and ∼10^5 acceleration in imaging time.

It is worth noting that hyperpolarization through our method requires relatively low laser (∼2mW/mg) and MW power (∼0.05mW/mg), where the estimates are reported for equivalent mass-weighted SNR to images presented here. Considering the saturation regime for a *single* 1μm diamond particle, we estimate a 30nW optical and 2nW MW power requirement respectively [19]. Due to the high mass of the particles here, our MRI experimental demonstrations were performed with laser power densities ∼80mW/mm^2, somewhat elevated above levels suitable for in-vivo operation (∼4.7mW/mm^2 [20]); indeed, laser power is not restrictive in preclinical settings since substantially lower masses are typically employed [21]. Moreover in our experiments, we estimate a specific absorption rate (SAR) of 1.1×10^4 W/kg[G]^2

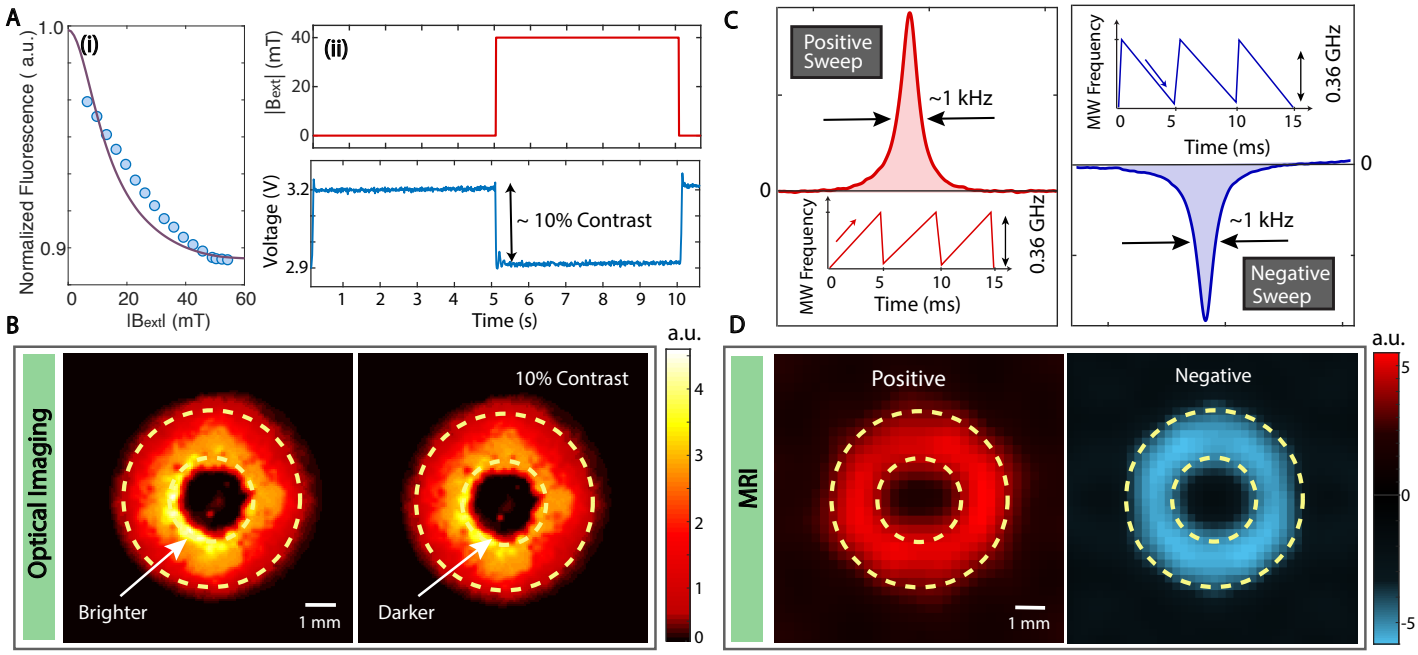

Figure 2. **On-demand dual-mode image modulation.** (A) (i) Normalized fluorescence signal for randomly oriented ensemble of diamond particles under an applied magnetic field (points: experiment, red-line: simulation). We ascribe the discrepancy to scattering effects. (ii) Optical modulation under 40±2mT pulsed magnetic field showing a signal contrast ∼10%. (B) *Optical images* under 0 and ∼40mT applied field showing weak ∼10% optical contrast. (C) ^{13}*C hyperpolarization sign control*. MW frequency sweeps in low-to-high (high-to-low) fashion across the NV ESR spectrum leads to a positive (negative) hyperpolarization. Shown are 7T ^{13}C NMR spectra under opposite sweep conditions. (D) ^{13}*C MR images* under opposite MW sweep conditions, showing full sign reversal and ∼194% modulation contrast. Here FLASH images were taken with TE=0.6ms and TR=500ms.

of MW power. At an electron Rabi frequency of ≈100kHz, broadly defining the regime of our operation, this corresponds to ≈14W/kg, which is close to the threshold of safe in-vivo operation (4W/kg [22]). We note that the hyperpolarization signal is highly robust to decrease in MW power, and scales approximately logarithmically with it [12], indicating that the SAR can be easily curtailed while maintaining relatively large NMR enhancement factors.

We use a variant of FLASH [23] to produce the MRI images at 9.4T (see Fig. 1F). To overcome the short T_2 ≈1ms of ^{13}C in diamond, the width of the radio frequency (RF) pulses and the gradient lobes are minimized to create a short echo time (0.5ms). Moreover, to eliminate any interference with the phase encoding gradient and distortions during the short RF pulses due to the relatively long (200μs) gradient switching periods, the imaging was performed without a slice selection gradient (Fig. 1B). This is also possible since we are primarily interested in projection images along the z-axis. The SNR of the MR image (Fig. 1F) is ∼4 in 16 scans, limited by rapid ^{13}C T_2 decay, low sample filling factor (≈0.0016) and laser-limited hyperpolarization. The use of line-narrowing sequences [24], such as spin-locking [25] or quadratic echos [26], can improve the imaging SNR by at least an order of magnitude. For in-vitro samples, the use of higher laser power close to saturation intensity (∼1W/mm^3) can increase the MR signal 10 times compared with the present results. Diamonds with higher ^{13}C content will provide larger signals, with the resulting SNR improvement scaling with enrichment [19]. Further improvements may be realized by optimizing the detection coil geometry and increasing of filling factor, for instance through the use of small volume inductively-coupled receiver coils [27, 28] matched to the sample under study. These concerted gains in MR signal (∼3 orders of magnitude) could also permit similar high-contrast images in nanosized particles (<100nm), material platforms that are most germane to in-vivo applications.

The MRI spatial resolution scales $\propto 1/(\gamma G_{\max}\tau)$, where γ is the gyromagnetic ratio, $G_{\max}$ and τ are the maximum gradient strength and the duration of its application. In our experiments, $G_{\max}$ = 950mT/m, leading to a resolution of 640μm in both dimensions. After zero-filling and smoothening, the pixel size presented in Fig. 1F has a square length of 160μm. Recent amplifier development that increase $G_{\max}$ can improve the spatial resolution [29, 30]. Of course, ultimately, the MR resolution can be just optical *diffraction-limited*, since only illuminated diamond particles contribute to any signal. One can envision beam-rastering modalities that buildup MR images pixel-by-pixel, in a manner that is solely resolution limited by optics.

We emphasize our optical DNP method presents several advantages when compared with traditional methods of hyperpolarization for solids imaging, employed for instance in ^{29}Si microparticles [31, 32]. We work at room temperature and low field (∼40 mT), and polarize samples in under 1min of laser pumping, as opposed to traditional high magnetic field ($\gtrsim$3T) and low temperature (<4K) approaches where polarization buildup can take several hours [33, 34]. While the absolute polarization is lower in our method, we circumvent the traditionally high polarization loss (as large as 99% [35]) accrued upon thawing and sample transfer out of the cryostat; ultimately, this results in a relatively high level of polarization delivery at the imaging source. Technologically too, our technique aids end-user operation – MW amplifiers and sweep sources are low-cost and readily available, empowering the construction of highly portable hyperpolarization devices that can retrofit to existing MRI scanners [19]. More importantly, since the high polarization is detection-field agnostic, our technique would open possibilities for continuous low-field MRI [36], along with

simultaneous optical imaging *in-situ*, particularly attractive because the hyperpolarization can be replenished optically.

Both optical and MRI modalities allow on-demand signal amplitude modulation, enabling common-mode suppression of background signals in both imaging dimensions. The fluorescence emission at moderately low fields, especially approaching 50mT, is strongly conditioned on the misalignment angle ϑ of the N-to-V axis to the applied field [37, 38]. This arises due of the mixing of the $m_s = \pm 1$ spin levels in the excited state, and since the randomly oriented particles sample all possible ϑ angles, allows a simple means to modulate the optical images by the pulsed application of an external field $\mathbf{B}_{ext}$ [16]. Following Ref. [37] we simulated the fluorescence dependence under application of $\mathbf{B}_{ext}$ (Fig. 2A (i)) using rate equations in a 7-level model of the NV center: $\frac{\mathrm{d}n_i}{\mathrm{d}t} = \sum_{j=1}^{7}(k_{ji}n_j - k_{ij}n_i)$, where n_i is the population of the $|i\rangle$ state, and k_{ij} denotes the kinetic transition rate between state $|i\rangle$ and $|j\rangle$ (measured in [37]). At steady state, the state population and consequent photoluminescence (red line in Fig. 2A (i), obtained evaluating $\int n_i(\mathbf{B}_{ext}, \vartheta)\sin\vartheta d\vartheta$) decreases with $\mathbf{B}_{ext}$, in reasonable agreement with the (normalized) experimental measurements (blue dots in Fig. 2A (ii)). In our imaging experiments, we modulate the optical images (Fig. 2C,D) by application of $\mathbf{B}_{ext}$ ~40 ±2mT, an identical field employed for hyperpolarization, and obtain a 10% optical modulation contrast. (Fig. 2A (ii)).

MRI amplitude modulation relies on the remarkable dependence of the ^{13}C hyperpolarization sign on the direction of MW sweeps, a feature originating in the rotating frame LZ dynamics excited by the chirped microwaves (Fig. 2B) [12, 18]. The ^{13}C nuclei are aligned (anti-aligned) with the polarization field under low-to-high (high-to-low) frequency sweeps over the NV ESR spectrum. Importantly, and contrary to optical modulation, this allows a *complete* sign-reversal of the MRI images at full contrast, all while requiring no additional infrastructure. Indeed, it is challenging to achieve such high signal modulation contrasts with conventional cryogenic DNP approaches, primarily due to technical limitations of MW cavity switching in these experiments [35, 39]. As a figure of merit, we characterize the modulation contrast as the difference ratio of the MR images $\mathcal{I}$ and $\overline{\mathcal{I}}$ under opposite MW sweeps positive and negative images (Fig. 2E-F) as: $\Delta = \frac{1}{N^2}\left(\frac{\mathcal{I}-\overline{\mathcal{I}}}{\mathcal{I}+\overline{\mathcal{I}}}\right)$, where N^2 is the total number of pixels. From the data in Fig. 2E-F, we obtain Δ =194 ± 0.3%. We ascribe the difference from full contrast to be arising from the imprecise repeatability of the pneumatic sample shuttler, an easily improvable feature, and irrelevant if the MR images are ultimately to be acquired at low-field [36, 40, 41]. In Ref. [19] for instance, we demonstrated Δ >198% for the hyperpolarized NMR signals.

Such high-contrast signal modulation opens the door to imaging the diamond particles with high SNR even while embedded in an overwhelmingly strong background. We refer to *background* in this context as media that have fluorescence *or* ^{13}C NMR signals that overlap in wavelength (or NMR frequency) with the diamond particles. As a proof of concept (Fig. 3), we consider particles being co-included with a high concentration of Alexa 647, a fluorescence dye which has a strong emission at 600nm, as well as [^{13}C]-methanol, which has a chemical shift nearly overlapping that of diamond. These solution media fill both the inner and outer spaces of the capillary tube that comprise the diamond phantom in Fig. 3A-B. The strong backgrounds result in images that are circle-shaped since the diamond phantom is completely indiscernible within it (Fig. 3C-D). To recover the diamond signals in the optical modality, we performed lock-in detection under application of a 40mT 0.1Hz square-wave modulated magnetic field.

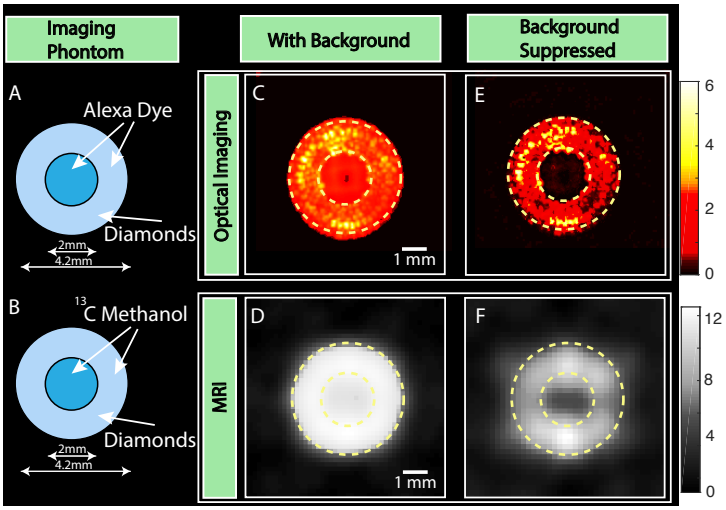

Figure 3. **Dual-mode background suppression.** (A-B) *Schematic of imaging phantoms*. Diamonds are arranged in ring-shaped phantom, co-situated with Alexa 647 dye and ^{13}C-methanol that present a strong artificial background for optical and MR imaging respectively. Diamond particles occupy the ring as in Fig. 2, while the solutions are present in all parts of the phantom. (C-D) Optical and MR images with the artificial background. Dashed lines serve as a guide to the eye for the imaging phantom. Diamond particles are indistinguishable from the background in both imaging dimensions. (E-F) *Background suppressed* optical and MR images employing signal modulation (reversal) allows the complete recovery of the original diamond phantom in both imaging modalities. Here the suppression factors are 2 and 5 respectively, although this could be an order of magnitude larger in both cases.

We recorded a 2000-frame movie at 0.1s frame rate, and computationally applied lock-in suppression on each pixel individually. The resulting image (Fig. 3E) shows good recovery of the diamond signal, in this case, from the 2 times larger background. Ultimately optical background suppression is limited by the optical contrast, and up to an order of magnitude is routinely experimentally feasible. Concurrent MRI background suppression is realized by subtracting the images under opposite sweep-ramp hyperpolarization conditions. Although the [^{13}C]-methanol signal herein was 5 times larger than the diamond signal, it is completely canceled (Fig. 3F). Indeed, hyperpolarization sign control allows one to address the diamond ^{13}C nuclei in exclusion of all other ^{13}C spins in the sample. The intrinsically high contrast of the diamond MRI sign-reversals, along with the low inherent tissue backgrounds at low-fields, augurs well for high-contrast in-situ MRI detection.

Efficiency gains through dual-mode imaging – Being able to co-register images in both optical and MR domains can yield SN enhancements, especially while imaging *in-tissue* settings. Optical fluorescence imaging requires the ability to illuminate the diamonds as well as collect the resulting fluorescence. While the diamond particles are quite optically bright, imaging through tissue presents a set of challenges that often dramatically restrict the proportion of photons that can be usably collected. Not only are there *round-trip* attenuation and scattering losses (scaling $\sim \lambda^{-4}$) to contend with, but additionally, the unusually high refractive index differential between diamond and its environment, and geometric solid angle constraints of the detector at high fields-of-view (FOVs) severely restrict the ultimate flux of collectable fluorescent photons. At 650nm through human tissue, for instance, attenuation and scattering lead to exponential signal losses with coeffi-

cients 0.1mm^{-1} and 1.1mm^{-1}, respectively [42, 43]. An order of magnitude calculation of the *chain* of losses from illumination-to-detection is quite revealing (see Supplementary Information [44]): *(i)* green-to-red photon conversion is rather inefficient, $\gtrsim 10^{-5}$ even at relatively low NV concentrations 0.1ppm [45] *(ii)* total internal reflection limits photon transmission and retrieval through the randomly oriented particles by a factor $\sim 10^{-3}$, *(iii)* round-trip attenuation losses cause signal suppression by as much as $\sim$0.3 through 5mm of tissue, *(iv)* while scattering affects the signal by an excess of $\sim 10^{-3}$ for the same tissue thickness, and finally, *(v)* finite numerical aperture detection limits photon collection by a further $\sim 10^{-2}$, here assuming a detection numerical aperature NA = 0.18. Put together, these losses can be considerable, and proscribe the ultimate efficiency of optical imaging in real tissue media.

An analogous analysis of hyperpolarized MR imaging indicates that it can be competitively efficient, especially with increasing tissue depth. In contrast to optical imaging, one only partakes of losses in the *one-way* illumination of the particles with 520nm light. Hyperpolarization efficiency is $\sim 2\times 10^{-4}$ per ^{13}C nucleus per incident photon [12]. The high detection losses and geometric solid-angle collection constraints are replaced by more benign factors related to sample-coil filling, detector Q, and the overall MR detection frequency [46]. Surface coils matched to the sample and the use of high-Q ferrite resonators can lead to substantially efficient detection [47, 48]. Indeed given the immunity to losses upon fluorescence scattering and attenuation, MR imaging can become preeminent even for buried particles relatively shallow in depth. If η were to be the ratio of optical and MR imaging SNR for *surface* diamond particles, MR imaging would have higher overall SNR than its optical counterpart at a depth $d \approx \frac{1}{1.2}\log(\eta)$ mm at 650nm, scaling logarithmically with the differential SNR ratio. Importantly, since both optical and MR imaging can proceed simultaneously, there are opportunities to use a "maximum-likelihood" hybrid of both modalities [49], wherein MR gains prominence with increasing depth profile.

Accelerated conjugate-space dual-mode imaging – Apart from reaping higher SNR, the ability of optical and MR imaging to capture the object simultaneously in Fourier-reciprocal spaces opens possibilities for significant imaging acceleration. As a specific example, we consider a typical wide field-of-view (FOV) imaging scenario where optical imaging is performed by rastering a low-power beam across the sample. This is germane to the imaging of embedded diamond particles in tissue. Simultaneous dual-mode imaging in real-space and k-space naturally provides the advantage that *every* sampled point in one space contains information from *all* the points in the other space. In the limit of imaging sparse objects in a wide FOV, and assuming that the imaging time cost is close to identical in both spaces, one could devise a hybrid protocol for sampling the FOV in both spaces simultaneously such that one rapidly converges to a high-fidelity image. Philosophically, this approach shares similarities with acceleration attainable through compressed sensing methods [50, 51]; in contrast, here we harness the ability to *directly* sample in both Fourier-conjugate spaces at once.

Fig. 4A describes one such imaging protocol. Given a sparse original image to be acquired, a subset ℓ k-space points are first sampled in each dimension. The resulting blurry low-k image is thresholded and *fed-forward* to confine real-space points to be sampled through optical means. At high sparsity s, defined herein as the fraction of zero pixels in the FOV, this can substantially reduce the number of points in real-space to be rastered over, and accelerate image acquisition. Fig. 4B presents an illustrative example of the protocol applied to an image with high sparsity, $(1-s)$ =0.0375. By employing ℓ=16 k-space samples in each dimension, and thresholding at 75% of the maximum, we obtain an imaging acceleration of 16, since large swathes of the (real-space) image do not need to be sampled over. We envision this hybrid mode being relevant to tumor-targeted diamond particles in-vivo, especially in endoscopic detection settings, where low-k MRI can serve as a guide to optical imaging [52].

Let us now analyze the regime of applicability and inherent trade-offs involved. In experimental settings, there is a time-cost to be accrued per sample (pixel) for both real-space (optical) as well as k-space (MR) imaging. For simplicity, we assume here that this time cost is identical for both imaging dimensions, although it is straightforward to scale the obtained results by the cost-ratio η as appropriate to the particular imaging setting. Given this, it is not surprising that there is an *optimal* k-space sample ℓ_{opt} that draws the compromise between better constraining real-space sampling, and taking longer to determine. This is demonstrated in Fig. 4C where, in a 32 $\times$ 32 pixel FOV, we consider the normalized imaging time savings over either modality for target images with varying sparsity. In these simulations, we perform statistics with 30 image configurations of fixed sparsity, assuming that the minimum feature size occupies one pixel. Fig. 4C demonstrates that hybrid sampling can deliver more than an order of magnitude in time savings (right axis), while only requiring the scanning of $\ell_{\text{opt}} \approx$10% of total k-space (upper axis), notwithstanding the relatively small FOV considered. As expected, ℓ_{opt} increases with decreasing sparsity, a reflection of larger k-samples required to account for the increasing image complexity (see Fig. 4D). Given the small FOV and discrete values of k-samples, this manifests in the staircase-like pattern in Fig. 4D, but scales $\ell_{\text{opt}} \propto (1-s)^{1/4}$ (solid line) as we shall derive below. Finally, in Fig. 4E we consider the combined imaging time τ under optimized conditions as a function of image sparsity, assuming that time for optical imaging is 1. Indeed, the imaging acceleration is quite substantial, scaling as $\tau^{-1} \propto (1-s)^{-1/2}$, and becoming increasingly utilitarian at high image sparsity.

It is revealing to consider the origins of this imaging acceleration by studying the *trajectory* of the reconstructed image as it approaches the target with each step of the protocol advancing (see Fig. 4F). Once again studying several image configurations with a fixed sparsity, we consider in Fig. 4F the overlap of the reconstructed image $\mathcal{I}'$ to the target image $\mathcal{I}$ through the correlation $\mathcal{C} = \sum (\mathcal{I} - \langle \mathcal{I} \rangle)(\mathcal{I}' - \langle \mathcal{I}' \rangle)$, where $\langle \cdot \rangle$ indicates the mean value. Indeed under usual rastered form of optical image acquisition (dashed green line in Fig. 4F), the reconstructed image *linearly* approaches the target as more samples are acquired. In contrast, employing the hybrid acquisition of a few k-space points, and by constraining the space over which the final image is to be acquired, one obtains a rapid convergence of the image with the target. Numerically, *slope* of convergence scales approximately $\propto (1-s)^{-1/2}$ (inset in Fig. 4F), indicating rapid gains can be amassed at high image sparsity.

To analytically elucidate the imaging acceleration gains at high sparsity (solid lines in Fig. 4D-E), let us consider the real-space target image $f(x,y)$, which in k-space is $\mathcal{F}[f] = \hat{f}(k_x, k_y)$, where $\mathcal{F}$ denotes a spatial Fourier transform. As k-space sampling now occurs just to ℓ-th order, one obtains the reconstructed image, $\hat{f}_l(k_x,k_y) = \hat{f}(k_x,k_y) \cdot \Pi\left(\frac{k_x}{W_{kx}}\right) \cdot \Pi\left(\frac{k_y}{W_{ky}}\right)$, where Π is a rectangular function representing sampling window with a side length of, for instance, $W_{kx} = \delta k_x \ell$, where $\delta k_x = 1/N_x$ is the k-space

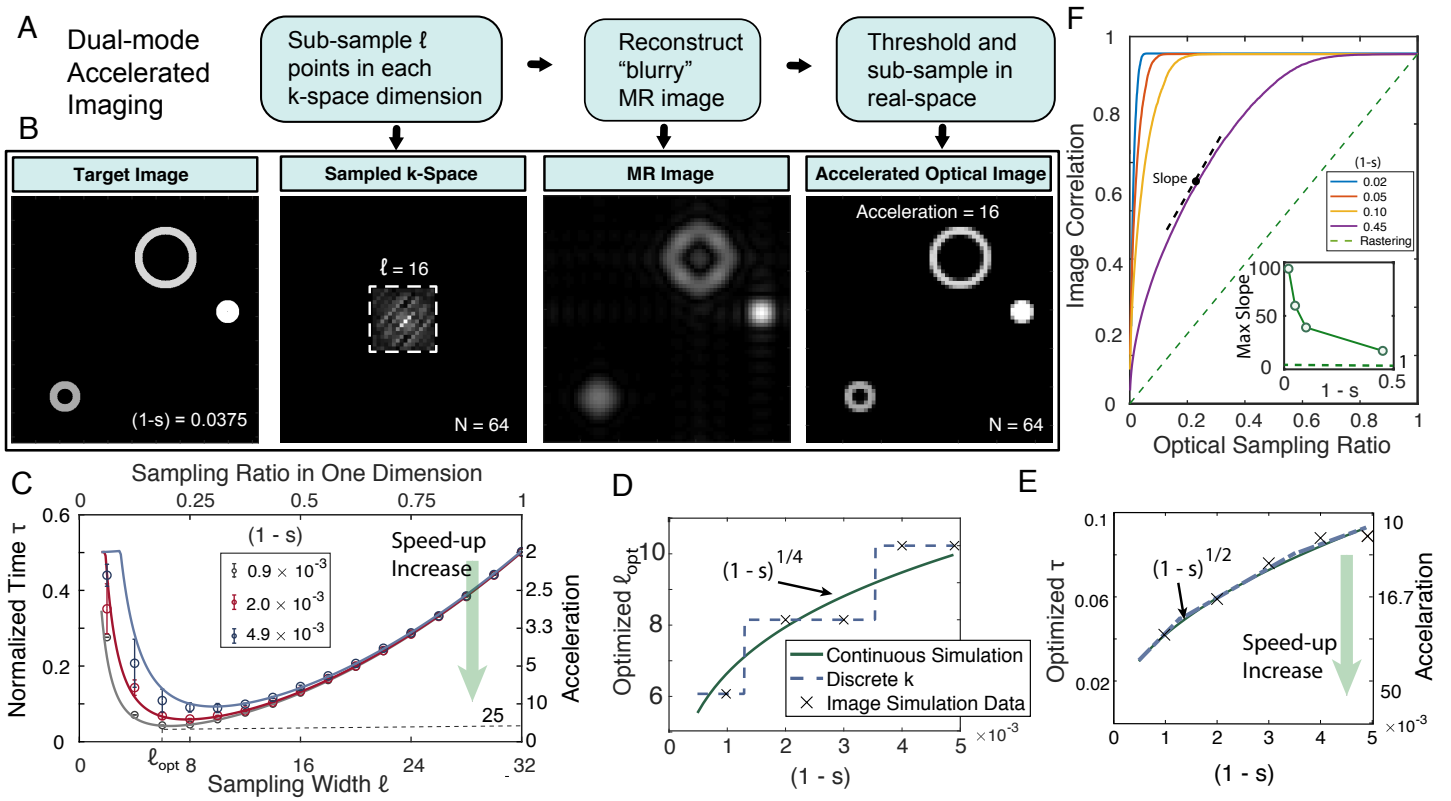

Figure 4. **Accelerated *x-k* conjugate-space imaging.** (A) *Protocol for accelerated imaging.* ℓ samples of the image are first acquired in k-space, and the resulting image upon thresholding is fed-forward to constrain the real-space points to be scanned over. (B) *Exemplary scenario* where the target image FOV consists of sparsely distributed objects, here simulated rings and circles of different sizes (far left panel). By sampling over ℓ=16 k-space points in each dimension, a blurry yet faithful image is formed of the target (center two panels), and can serve to restrict real-space sampling (right panel). (C) *Normalized imaging time* τ with different values of ℓ for images in a 32^2 pixel square FOV of different sparsity factors, and assuming identical time-costs per pixel in both conjugate space dimensions. Right axis indicates corresponding imaging acceleration. Here images consisted of unit-pixel objects, and we averaged over 30 random image configurations with identical sparsity; error bars denote standard deviations. The presence of an optimal k-space sample threshold $\ell_{\rm opt}$ is evident, stemming from a compromise between better confinement in real-space imaging, and associated time-cost for k-space imaging. (D) *Scaling of* ℓ_{opt} with image sparsity, showing that more k-space values are required to account for increasing imaging complexity. Points: given discrete possible values of k, $\ell_{\rm opt}$ has a staircase-like behavior. Solid line: scaling of $\ell_{\rm opt}$ assuming continuous k values. (E) *Optimized imaging acceleration* through sampling $\ell_{\rm opt}$ points, showing more than an order of magnitude time savings at high sparsity. (F) *Trajectory of image convergence* quantified by image correlation $\mathcal{C}$ with protocol advancement. Green dashed line shows linear convergence under conventional optical rastering. In contrast, hybrid sampling in conjugate spaces can lead to rapid image convergence. *Inset:* Slope of image approach rapidly increases with image sparsity.

pixel size. Transformation back to real-space gives the convolution, $\mathcal{F}^{-1}[\hat{f}] = f(x,y) * (W_{kx}\text{sinc}(W_{kx}x)\cdot W_{ky}\text{sinc}(W_{ky}y))$. Indeed considering the imaging point spread function $f(x,y) = \delta(x,y)$, and assuming for simplicity a square image FOV, we obtain $\mathcal{F}^{-1}[\hat{f}] = \text{sinc}(x\delta k\ell)\text{sinc}(y\delta k\ell)$. Hence an object of pixel radius r is effectively blurred $r \to r_0\left(\frac{N}{\ell}\right)$, where the factor r_0 is set by the thresholding level employed (see Supplementary Information [44]), and ℓ/N is the effective k-space sampling ratio. Indeed, the k-space imaging constrains the area required for subsequent optical scanning to just this blurred region; increasing ℓ makes a more faithful representation and improves regional constraints, but comes is associated with a time-cost. To evaluate the time savings as a result of this hybrid strategy, let us for simplicity now consider the FOV consists of n_d objects of radius r, giving $(1-s) = n_d\pi r^2/N^2$. The normalized imaging time is then, $\tau = \left[(1-s) + \frac{2r_0}{N}\frac{1}{\ell}\left(\frac{1-s}{r}\right) + \frac{r_0}{\ell^2}\left(\frac{1-s}{r^2}\right) + \frac{\ell^2}{N^2}\right]$ [44]. In the limit of high sparsity, $(1-s)/r \to 0$, and $(1-s)/r^2 \to \mathcal{O}(1)$, giving $\tau \approx C_0\frac{(1-s)}{\ell^2} + \frac{1}{N}\ell^2$, where $C_0 = \frac{r_0}{r^2}$ is a constant. Determining the optimal ℓ to minimize τ, gives, $\ell_{\rm opt} \propto (1-s)^{1/4}$, and the optimal (normalized) time $\tau \propto (1-s)^{1/2}$. The scaling from this simple model is shown as the solid lines in Fig. 4D-E and are a close match to the numerical results especially at the limit of high image sparsity. Here we considered the image to consist of unit pixel objects ($2r = 1$), with no constraints on their relative placement in the image FOV. Moreover, while we have restricted our attention here to 2D images, identical acceleration gains are attainable even for 3D imaging [44].

In summary therefore, leveraging Fourier conjugate sampling, even a simple protocol like the one in Fig. 4A can deliver remarkable gains at high image sparsity ($s \to 1$). The *combined* image acceleration scales $\tau^{-1} \propto (1-s)^{-1/2}$, while only requiring the scanning of a minuscule percentage of k-space $\ell_{\rm opt} \propto (1-s)^{1/4}$, and leading to an approach to the target image whose slope scales $\propto (1-s)^{-1/2}$ with each step of the protocol. Indeed, since this scenario is strongly operational in real-world targeted nanodiamond imaging applications, where sparsity factors s >95% [53, 54] are typical, we anticipate that these strong acceleration gains are well within reach in practical settings. Since in principle the optical imaging can be performed *during* MR imag-

ing, several possibilities exist for the protocol in Fig. 4 to itself be further augmented.

Conclusions and outlook – We have demonstrated a new means of dual-mode imaging in diamond microparticles, and shown that a slew of complimentary advantages can be harnessed by marrying together visible optical and ^{13}C MR imaging. The biocompatible particles we employ are endowed with a high density NV defect centers. The same optical excitation that causes high-luminosity visible fluorescence from the NVs also serves to spin-polarize the lattice ^{13}C nuclei making the particles light up in MR imaging. We demonstrated MR signal enhancements by $\sim$204 over 9.4T under weak ($\sim$80mW/mm^2) optical illumination, and simultaneously bright optical florescence. We also demonstrated the ability to modulate the signals on-demand from both modalities, enabling a high-degree of background suppression in both optical and MR dimensions. Co-registering optical and MR images portends high-SNR imaging, especially for samples embedded in tissue and other scattering media, whereupon the MR modality can prove competitively efficient since it is largely immune to photon detection losses. Importantly, imaging in optical and MRI domains inherently occurs in Fourier-conjugate spaces, and allows us to develop hybrid protocols that feed-forward information from one domain to another to vastly accelerate image acquisition. For pertinent scenarios of imaging targeted particles in-vivo, where the wide-field images are highly sparse, we demonstrated the potential to accelerate image acquisition by about two orders of magnitude.

While the results contained herein largely constitute proof-of-concept demonstrations, several straightforward pathways exist through which imaging SNR in both modes can be enhanced further. In particular, materials advances would boost MR image SNR by two orders of magnitude through ^{13}C enrichment and other sample processing that improve the hyperpolarizability of the diamond particles. Especially exciting amongst them are new methods for diamond rapid thermal annealing (RTA) at elevated temperatures ($\sim$1700-1750°C) [55] that have been shown to substantially boost hyperpolarization enhancement levels (in some cases by an order of magnitude), as well as ^{13}C T_1 times, by suppressing deleterious lattice paramagnetic impurities. Such MR and optical imaging in-situ at low field might open exciting avenues for continuously optically replenishable imaging across both dimensions and might serve as a valuable targeting tool for several diagnostic and therapeutic avenues. Finally the high surface area diamond particles present an attractive platform through which the hyperpolarization could be transferred out into the targeting groups, potentially making them *chemically-functional* dual-mode imaging agents.

We focus finally on a particularly compelling application for dual-mode imaging diamond particles in *MRI-guided* endoscopy during colonoscopy [56]. Estimates show that colonoscopy misses up to 22% of adenomas, irrespective of size, and up to 2% of adenomas equal to or greater than 10mm [57]. While targeted fluorescence molecular imaging (FMI) has been suggested as a means to detect premalignant neoplasms and cancerous lesions in colorectal cancer screening [58–60], it cannot provide sufficient resolution for a signal collected from mm-deep location nor a complete 3D picture of the tumor. Instead, targeting nanodiamonds can label malignant lesions spread deeper into tissue. A simple optical fiber (power $\approx$10mW) fitted on the endoscope would serve to illuminate these particles in-vivo, enabling their imaging directly optically through the endoscope, as well as through low-field MRI. Given the high inherent 3D FOV possible through MRI, *malignancy-maps* obtained from MRI could potentially aid in on-site optical endoscopy examination and lower experiential dependence, which currently plays an important role in the lesion detection rate. Moreover, by employing hyperpolarized diamond particles as major elements in MRI-guided needle tracking during, for e.g. biopsy of deep organs, would increase a visibility of needles and/or catheters in MRI images. Visualization of passive needles is based on their materials properties and is prone to imaging artefacts and inadequate tracking, while a recently emerging active MRI catheter devices [61] are based on incorporation of fiducial markers along the needle profile to accomplish greater MRI visibility. Modulation of fluorescent and MRI signals from diamond particles open perspectives for completely background free tracking of catheters devices in-vivo.

Acknowledgments – It is a pleasure to gratefully acknowledge discussions with and/or technical contributions of D. Barskiy, S. Conolly, B. Gilbert, M. Lustig, R. Nirodi, G. Palmer, A. Shames, D. Suter and M. Torelli. This material is based in part upon work supported by the National Science Foundation Grant No. 1903803. C.A.M. acknowledges support from the National Science Foundation through grants NSF-1547830, NSF-1903839, and from Research Corporation for Science Advancement through a FRED Award. O.S. acknowledges partial support from the National Cancer Institute of the National Institutes of Health under Award No. R43CA232901.

Materials and Methods – Experiments were performed with $\sim$200μm diamond powders (average edge length 87$\pm$3.9 μm) with $\sim$1 ppm NV from Element6. While these particles provided high hyperpolarization enhancements ($\sim$280 at 7T), we have observed hyperpolarization enhancements factors of $\sim$3 for 100nm particles containing $\sim$3ppm of NV centers. A detailed discussion of material factors affecting ^{13}C hyperpolarization will be presented elsewhere. The mass of the sample used in all the experiments is $\sim$40μg. For uniform illumination of the high mass samples, in the optical imaging is performed under simultaneous excitation from four 520nm fiber-coupled laser diodes (Lasertack) in a rhomboidal configuration, and the florescence imaged on a CMOS detector (Thorlabs DCC1645C) through a 594nm long pass filter (Semrock BLP01-594R-25).

The hyperpolarization apparatus contains laser excitation, microwave irradiation and weak electro-magnet to fine-tune the polarization field. We employ a miniature 1W 520nm diode laser (Lasertack PD-01289) in a feedback loop with an integrated thermoelectric cooler for adequate thermal control (TE Inc. TE-63-1.0-1.3). Microwaves are generated by miniature voltage controlled oscillator (VCO) sources (Minicircuits ZX95-3800A+, 1.9-3.7GHz, output power p = 3.1dBm). Frequency sweeps are produced by controlling the VCO frequency by a homebuilt quad-channel voltage ramp generator controlled by a PIC microprocessor (PIC30F2020). The sweep generator employs dual multiplying digital-to-analog convertors (MDACs, Linear Technology LTC1590) to generate the sawtooth voltage ramps. All MR images are taken with the particles immersed in water or solution.

A pneumatic field-cycling device was implement to enable rapid sample transfer from low field (40mT) to high a wide-bore 9.4T Bruker DRX MRI machine, within which a 10 mm ^{1}H/^{13}C Volume Coil is installed. The shuttling device is composed of a quartz channel transporting the sample, a concave-shape stopper at the end of the channel, and driven by a vacuum machine to transfer the sample in under 1s.

[1] D.-E. Lee, H. Koo, I.-C. Sun, J. H. Ryu, K. Kim, and I. C. Kwon, Chemical Society Reviews **41**, 2656 (2012).
[2] B. P. Abbott, R. Abbott, T. Abbott, F. Acernese, K. Ackley, C. Adams, T. Adams, P. Addesso, R. Adhikari, V. Adya, *et al.*, Astrophys. J. Lett **848**, L12 (2017).
[3] G. Welch, G. Bishop, *et al.*, (1995).
[4] S. Mutic and J. F. Dempsey, in *Seminars in radiation oncology*, Vol. 24 (Elsevier, 2014) pp. 196–199.
[5] Z. Tovar-Spinoza, D. Carter, D. Ferrone, Y. Eksioglu, and S. Huckins, Child's Nervous System **29**, 2089 (2013).
[6] A. Oto, I. Sethi, G. Karczmar, R. McNichols, M. K. Ivancevic, W. M. Stadler, S. Watson, and S. Eggener, Radiology **267**, 932 (2013).
[7] T. Zhang, A. Neumann, J. Lindlau, Y. Wu, G. Pramanik, B. Naydenov, F. Jelezko, F. Schuder, S. Huber, M. Huber, *et al.*, Journal of the American Chemical Society **137**, 9776 (2015).
[8] Y. Wu, F. Jelezko, M. B. Plenio, and T. Weil, Angewandte Chemie International Edition **55**, 6586 (2016).
[9] V. Vaijayanthimala, D. K. Lee, S. V. Kim, A. Yen, N. Tsai, D. Ho, H.-C. Chang, and O. Shenderova, Expert opinion on drug delivery **12**, 735 (2015).
[10] F. Jelezko and J. Wrachtrup, Physica Status Solidi (A) **203**, 3207 (2006).
[11] R. Fischer, C. O. Bretschneider, P. London, D. Budker, D. Gershoni, and L. Frydman, Physical review letters **111**, 057601 (2013).
[12] A. Ajoy, K. Liu, R. Nazaryan, X. Lv, P. R. Zangara, B. Safvati, G. Wang, D. Arnold, G. Li, A. Lin, *et al.*, Sci. Adv. **4**, eaar5492 (2018).
[13] A. E. Dementyev, D. G. Cory, and C. Ramanathan, Phys. Rev. Lett. **100**, 127601 (2008).
[14] E. Rej, T. Gaebel, T. Boele, D. E. Waddington, and D. J. Reilly, Nature communications **6** (2015).
[15] A. Ajoy, B. Safvati, R. Nazaryan, J. Oon, B. Han, P. Raghavan, R. Nirodi, A. Aguilar, K. Liu, X. Cai, *et al.*, arXiv preprint arXiv:1902.06204 (2019).
[16] A. Bumb, S. K. Sarkar, X. Wu, K. A. Sochacki, P. Kellman, M. W. Brechbiel, and K. C. Neuman, Biophysical Journal **106**, 796a (2014).
[17] A. Ajoy, R. Nazaryan, K. Liu, X. Lv, B. Safvati, G. Wang, E. Druga, J. Reimer, D. Suter, C. Ramanathan, *et al.*, Proceedings of the National Academy of Sciences **115**, 10576 (2018).
[18] P. R. Zangara, S. Dhomkar, A. Ajoy, K. Liu, R. Nazaryan, D. Pagliero, D. Suter, J. A. Reimer, A. Pines, and C. A. Meriles, Proceedings of the National Academy of Sciences , 201811994 (2019).
[19] A. Ajoy, R. Nazaryan, E. Druga, K. Liu, A. Aguilar, B. Han, M. Gierth, J. T. Oon, B. Safvati, R. Tsang, *et al.*, arXiv preprint arXiv:1811.10218 (2018).
[20] M. L. Denton, M. S. Foltz, L. E. Estlack, D. J. Stolarski, G. D. Noojin, R. J. Thomas, D. Eikum, and B. A. Rockwell, Investigative ophthalmology & visual science **47**, 3065 (2006).
[21] D. Ho, C.-H. K. Wang, and E. K.-H. Chow, Science Advances **1**, e1500439 (2015).
[22] I. E. Commission *et al.*, IEC 60601-2-33 Ed. 3.0 (2010).
[23] A. Haase, Magnetic Resonance in Medicine **13**, 77 (1990).
[24] U. Haeberlen, *High Resolution NMR in Solids: Selective Averaging* (Academic Press Inc., New York, 1976).
[25] W.-K. Rhim, D. Burum, and D. Elleman, Physical Review Letters **37**, 1764 (1976).
[26] M. A. Frey, M. Michaud, J. N. VanHouten, K. L. Insogna, J. A. Madri, and S. E. Barrett, Proceedings of the National Academy of Sciences **109**, 5190 (2012).
[27] D. Sakellariou, G. Le Goff, and J.-F. Jacquinot, Nature **447**, 694 (2007).
[28] A. Hai, V. C. Spanoudaki, B. B. Bartelle, and A. Jasanoff, Nature biomedical engineering **3**, 69 (2019).
[29] J. Sabate, L. J. Garces, P. M. Szczesny, Q. Li, and W. F. Wirth, in *2004 IEEE 35th Annual Power Electronics Specialists Conference (IEEE Cat. No. 04CH37551)*, Vol. 1 (IEEE, 2004) pp. 261–266.
[30] D. Seeber, J. Hoftiezer, W. Daniel, M. Rutgers, and C. Pennington, Review of Scientific Instruments **71**, 4263 (2000).
[31] M. Cassidy, H. Chan, B. Ross, P. Bhattacharya, and C. M. Marcus, Nature nanotechnology **8**, 363 (2013).
[32] J. W. Aptekar, M. C. Cassidy, A. C. Johnson, R. A. Barton, M. Lee, A. C. Ogier, C. Vo, M. N. Anahtar, Y. Ren, S. N. Bhatia, *et al.*, ACS nano **3**, 4003 (2009).
[33] T. Maly, G. T. Debelouchina, V. S. Bajaj, K.-N. Hu, C.-G. Joo, M. L. MakJurkauskas, J. R. Sirigiri, P. C. A. van der Wel, J. Herzfeld, R. J. Temkin, and R. G. Griffin, The Journal of Chemical Physics **128**, 052211 (2008).
[34] C. O. Bretschneider, Ü. Akbey, F. Aussenac, G. L. Olsen, A. Feintuch, H. Oschkinat, and L. Frydman, ChemPhysChem **17**, 2691 (2016).
[35] D. E. Waddington, T. Boele, E. Rej, D. R. McCamey, N. J. King, T. Gaebel, and D. J. Reilly, Scientific reports **9**, 5950 (2019).
[36] M. Sarracanie, C. D. LaPierre, N. Salameh, D. E. Waddington, T. Witzel, and M. S. Rosen, Scientific reports **5**, 15177 (2015).
[37] J. Tetienne, L. Rondin, P. Spinicelli, M. Chipaux, T. Debuisschert, J. Roch, and V. Jacques, New Journal of Physics **14**, 103033 (2012).
[38] Y.-X. Liu, A. Ajoy, P. Cappellaro, *et al.*, Physical review letters **122**, 100501 (2019).
[39] L. R. Becerra, G. J. Gerfen, R. J. Temkin, D. J. Singel, and R. G. Griffin, Physical Review Letters **71**, 3561 (1993).
[40] C. Goetz, E. Breton, P. Choquet, V. Israel-Jost, and A. Constantinesco, Journal of Nuclear Medicine **49**, 88 (2008).
[41] D. E. Waddington, M. Sarracanie, H. Zhang, N. Salameh, D. R. Glenn, E. Rej, T. Gaebel, T. Boele, R. L. Walsworth, D. J. Reilly, *et al.*, Nature communications **8**, 15118 (2017).
[42] S. L. Jacques, OSA TOPS on advances in optical imaging and photon migration **2**, 364 (1996).
[43] T. Lister, P. A. Wright, and P. H. Chappell, Journal of biomedical optics **17**, 090901 (2012).
[44] See supplementary online material.
[45] H. Clevenson, M. E. Trusheim, C. Teale, T. Schröder, D. Braje, and D. Englund, Nature Physics **11**, 393 (2015).
[46] D. Hoult, Progress in Nuclear Magnetic Resonance Spectroscopy **12**, 41 (1978).
[47] J. J. Ackerman, T. H. Grove, G. G. Wong, D. G. Gadian, and G. K. Radda, Nature **283**, 167 (1980).
[48] A. Haase, W. Hänicke, and J. Frahm, Journal of Magnetic Resonance (1969) **56**, 401 (1984).
[49] P. Thibault and M. Guizar-Sicairos, New Journal of Physics **14**, 063004 (2012).
[50] D. L. Donoho *et al.*, IEEE Transactions on information theory **52**, 1289 (2006).
[51] M. Lustig, D. Donoho, and J. M. Pauly, Magnetic Resonance in Medicine: An Official Journal of the International Society for Magnetic Resonance in Medicine **58**, 1182 (2007).
[52] R. T. Blanco, R. Ojala, J. Kariniemi, J. Perälä, J. Niinimäki, and O. Tervonen, European journal of radiology **56**, 130 (2005).
[53] A. M. Schrand, S. A. C. Hens, and O. A. Shenderova, Critical reviews in solid state and materials sciences **34**, 18 (2009).
[54] V. N. Mochalin, O. Shenderova, D. Ho, and Y. Gogotsi, Nature nanotechnology **7**, 11 (2012).
[55] L. Dei Cas, S. Zeldin, N. Nunn, M. Torelli, A. I. Shames, A. M. Zaitsev, and O. Shenderova, Advanced Functional Materials , 1808362 (2019).
[56] V. Subramanian and K. Ragunath, Clinical Gastroenterology and Hepatology **12**, 368 (2014).
[57] P. C. van der Wel, K.-N. Hu, J. Lewandowski, and R. G. Griffin, Journal of the American Chemical Society **128**, 10840 (2006).
[58] J. J. Tjalma, P. B. Garcia-Allende, E. Hartmans, A. G. T. van

Scheltinga, W. Boersma-van Ek, J. Glatz, M. Koch, Y. J. van Herwaarden, T. M. Bisseling, I. D. Nagtegaal, *et al.*, Journal of Nuclear Medicine **57**, 480 (2016).

[59] E. Hartmans, J. J. Tjalma, M. D. Linssen, P. B. G. Allende, M. Koller, A. Jorritsma-Smit, *et al.*, Theranostics **8**, 1458 (2018).

[60] Y. Miyamoto, N. Muguruma, S. Fujimoto, Y. Okada, Y. Kida, F. Nakamura, K. Tanaka, T. Nakagawa, S. Kitamura, K. Okamoto, *et al.*, Cancer science **110**, 1921 (2019).

[61] N. Whiting, J. Hu, J. V. Shah, M. C. Cassidy, E. Cressman, N. Z. Millward, D. G. Menter, C. M. Marcus, and P. K. Bhattacharya, Scientific reports **5**, 12842 (2015).